ACS APPLIED MATERIALS & INTERFACES

Research Article

www.acsami.org

Bifunctional Modification of Graphitic Carbon Nitride with $MgFe_2O_4$ for Enhanced Photocatalytic Hydrogen Generation

Jie Chen, Daming Zhao, Zhidan Diao, Miao Wang, Liejin Guo, and Shaohua Shen*

International Research Center for Renewable Energy, State Key Laboratory of Multiphase Flow in Power Engineering, Xi'an Jiaotong University, Shaanxi 710049, China

Supporting Information

ABSTRACT: To gain high photocatalytic activity for hydrogen evolution, both charge separation efficiency and surface reaction kinetics must be improved, and together would be even better. In this study, the visible light photocatalytic hydrogen production activity of graphitic carbon nitride (g-C_3N_4) was greatly enhanced with $MgFe_2O_4$ modification. It was demonstrated that $MgFe_2O_4$ could not only extract photoinduced holes from g-C_3N_4, leading to efficient charge carrier separation at the g-C_3N_4/$MgFe_2O_4$ interface, but also act as an oxidative catalyst accelerating the oxidation reaction kinetics at g-C_3N_4 surface. This dual function of $MgFe_2O_4$ thus contributed to the great improvement (up to three-fold) in photocatalytic activity for hydrogen generation over g-C_3N_4/$MgFe_2O_4$ as compared to pristine g-C_3N_4, after loading Pt by photoreduction method. It was revealed that in the Pt/g-C_3N_4/$MgFe_2O_4$ system, the photoinduced electrons and holes were entrapped by Pt and $MgFe_2O_4$, respectively, giving rise to the promoted charge separation; moreover, as evidenced by electrochemical analysis, the electrocatalysis effect of $MgFe_2O_4$ benefited the oxidation reaction at g-C_3N_4 surface.

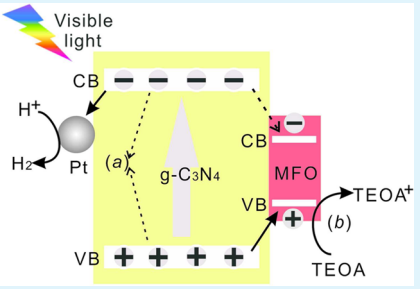

KEYWORDS: *solar hydrogen conversion, bifunctional modification, graphitic carbon nitride, ferrites, heterojunction*

1. INTRODUCTION

The scalable storage of solar energy by means of photocatalytically converting water to hydrogen fuels (H_2) hinges on fundamental improvements in photocatalysts.[1,2] Since the pioneering work of coupling a TiO_2 anode with a platinum dark cathode for photoelectrocatalytic water splitting by Fujishima and Honda in 1972,[3] extensive efforts have been devoted to constructing efficient photocatalytic/photoelectrocatalytic water-splitting systems. Although many semiconductor materials are capable of photocatalytically splitting water to produce hydrogen and/or oxygen, the solar energy conversion efficiency is still far from practical application, mainly because the three crucial steps for the water splitting reaction, i.e., solar light absorption, charge separation, and transportation, and surface catalytic reduction and oxidation reactions, are not efficient enough.[4] The polymer semiconductor, graphitic carbon nitride (g-C_3N_4), as a narrow band gap semiconductor material (band gap ~2.7 eV) can harvest solar light efficiently.[5] In addition, it has suitable band positions, i.e., conduction band (CB) of −0.9 V and valence band (VB) of +1.8 V versus reversible hydrogen electrode (RHE), for both H_2 and O_2 production and stable chemical properties, rendering it to be a promising material for photocatalytic water splitting.[6] However, the quick recombination of photoinduced electrons and holes greatly limits the photocatalytic activity of pure g-C_3N_4.[7−11] Therefore, facilitating the charge carriers separation and accelerating the surface redox reactions are urgently needed for improving the photocatalytic performance of g-C_3N_4.

Constructing semiconducting heterojunctions has been proven an effective way to facilitate the charge carriers separation, for example, in the most studied TiO_2/ZnO,[12,13] CdSe/CdS[14,15] heterojunctions, and TiO_2/CdS[16] heterojunctions, the charge carriers are efficiently separated in both of the semiconductor components driven by their proper band alignments and remarkably high quantum efficiencies for hydrogen production were then achieved. However, in these heterojunctions, the coupled semiconductors only functioned to separate the charge carriers, and even if the photocatalytic hydrogen evolution performances have been improved, the ability of the second semiconductors to electrocatalytically accelerate the catalytic oxidative reaction has seldom been taken into consideration. Therefore, it is supposed that coupling a semiconductor which can not only facilitate the separation of the photoinduced charge carriers, but also act as the oxidative electrocatalyst accelerating the oxidation reaction kinetics, will lead to further improvement of the photocatalytic efficiency. As for the g-C_3N_4-based heterostructures, by coupling with a second semiconductor (e.g., Cu_2O,[17] N-CeO_x[18]) for promoted charge separation and loading Pt or MoS_2[11,19] as the reductive hydrogen evolution cocatalyst (HEC), greatly enhanced photocatalytic hydrogen production activities have been achieved. While no evidence has shown that the second semiconductors were capable of electrocatalytically

Received: June 26, 2015
Accepted: August 3, 2015
Published: August 3, 2015

DOI: 10.1021/acsami.5b05714
ACS Appl. Mater. Interfaces 2015, 7, 18843−18848

accelerating the oxidative reaction kinetics. On the basis of the above concerns, it is proposed that coupling a bifunctional semiconductor with the abilities to separate the photoinduced charge carriers driven by the intrinsic band alignment with g-C_3N_4 and to act as oxidative catalyst to accelerate the oxidation reaction kinetics, will certainly further improve the photocatalytic hydrogen production activity of g-C_3N_4.

The spinel ferrites family has been proven to have interesting photocatalytic and photoelectrochemical properties for water splitting. In particular, $MgFe_2O_4$, $CaFe_2O_4$, and $ZnFe_2O_4$ have provided good examples for water oxidation reactions by facilitating the oxidative reaction in the Co−Fe_2O_3/$MgFe_2O_4$,[20] TaON/$CaFe_2O_4$,[21] and α-Fe_2O_3/$ZnFe_2O_4$[22] heterojunctions, respectively. In these heterojunctions, the photoinduced holes transferred from the VB of the substrate semiconductors (i.e., Co−Fe_2O_3, TaON, α-Fe_2O_3) to the VB of the ferrites due to the more negative VB positions of the ferrites, leading to efficient charge carrier separation. Moreover, the surface catalytic oxidation reactions were also promoted due to the excellent oxidative ability of the ferrites. Thus, higher photocatalytic water splitting efficiencies were obtained over these semiconductor/ferrite heterojunctions.

Herein, in this study, one of the earth-abundant ferrites of the spinel structure, i.e., spinel $MgFe_2O_4$ was used to modify g-C_3N_4. Due to the type I band alignment between $MgFe_2O_4$ and g-C_3N_4, the photoinduced holes migrated from g-C_3N_4 to $MgFe_2O_4$, facilitating the charge carriers separation in g-C_3N_4. Moreover, the surface catalytic oxidative reaction of g-C_3N_4/$MgFe_2O_4$ was also accelerated due to the electrocatalytic oxidation effect of $MgFe_2O_4$. The photocatalytic hydrogen production efficiency of g-C_3N_4 was then greatly improved by the dual function of $MgFe_2O_4$ on charge separation and electrocatalysis, with Pt loaded as hydrogen evolution cocatalyst. To investigate the effect of $MgFe_2O_4$ along with Pt on the photoactivity of g-C_3N_4, detailed characterization on the morphology, structure, and optical properties of the photocatalysts were carried out.

2. RESULTS AND DISCUSSION

$MgFe_2O_4$ particles were synthesized by the widely used sol−gel and autocombustion method.[23] The $MgFe_2O_4$ loaded g-C_3N_4 photocatalysts were prepared by a facile one-pot method by annealing the mixture of the obtained $MgFe_2O_4$ particles and melamine as the g-C_3N_4 precursor (see experimental details in the Supporting Information, SI). The obtained g-C_3N_4/$MgFe_2O_4$ photocatalysts were denoted as CN/MFO-*X* (*X* = 30, 90, 150, 210, 300), where *X* represents the amounts of $MgFe_2O_4$ particles (30, 90, 150, 210, 300 mg) used in the one-pot preparation process. The crystal structure of the as-prepared g-C_3N_4/$MgFe_2O_4$ photocatalysts was investigated by X-ray diffraction (XRD, Figure S1). g-C_3N_4 exhibits a typical graphitic interlayer (002) peak with d = 0.327 nm (27.4°) and a pronounced peak corresponding to the in-plane structural packing motif at 13.2°.[24,25] These two peaks are gradually decaying with increasing amounts of $MgFe_2O_4$ in the CN/MFO-*X* photocatalysts, which reflects a decrease of the long-range order of g-C_3N_4[26] and a host−guest interaction of g-C_3N_4 with $MgFe_2O_4$. $MgFe_2O_4$ are of spinel structure, belonging to the cubic phase (JCPDS No. 00-017-0464).[23] The characteristic peak intensities of $MgFe_2O_4$ are gradually increased with increasing amounts of $MgFe_2O_4$, proving the successful loading of $MgFe_2O_4$ on g-C_3N_4.The average size of the $MgFe_2O_4$ particles was estimated to be ca. 67.3 nm as calculated from the Scherer equation (see SI for the calculation details). In addition, the BET surface area and pore volume (Figure S2, Table S1) were enlarged after loading $MgFe_2O_4$ onto g-C_3N_4, which was largely attributed to the good spreading of $MgFe_2O_4$ on g-C_3N_4 and that the bulk phase of g-C_3N_4 was propped open with the ca. 67.3 nm $MgFe_2O_4$ particles embedding. However, with regard to the CN/MFO-*X* (*X* = 30, 90, 150, 210, 300) photocatalysts, it can be seen that their surface areas and pore distribution are almost the same, indicating that this macroscopic physical characterization of surface area would not account for the different photocatalytic hydrogen production performances of CN/MFO-*X* with varied *X* values.

The morphology of g-C_3N_4/$MgFe_2O_4$ was investigated by transmission electron microscopy (TEM) and high-angle annular dark-field scanning transmission electron microscopy (HAADF-STEM) as shown in Figure 1. As seen from Figure 1a, in the CN/MFO-150 photocatalysts, $MgFe_2O_4$ particles with irregular shape are dispersed on the surface of g-C_3N_4, whereas with increasing amounts of $MgFe_2O_4$, $MgFe_2O_4$ particles turned out to be aggregated, covering larger areas instead of spreading well on the substrate g-C_3N_4 photocatalyst (see the TEM images of all the CN/MFO-*X* photocatalysts in Figure S3). It was supposed that the aggregated $MgFe_2O_4$ particles overlapping g-C_3N_4 would be detrimental to the photocatalytic activity for hydrogen production by blocking the light absorption and shading the active sites on the g-C_3N_4 surface.[10,24,25,27] The size of the $MgFe_2O_4$ particles are ca. 80−100 nm, which is close to the calculated value from the Scherer equation. A high resolution TEM image (Figure 1b) collected from the $MgFe_2O_4$ part of Figure 1a displays an interplanar spacing of 0.25 nm, which corresponds to the *d*-spacing of (311) plane of $MgFe_2O_4$. To further evaluate the formation and composition of $MgFe_2O_4$, point scan EDX spectra of two areas in CN/MFO-150 with (*point 1*, Figure 1c) or without (*point 2*, Figure 1d) $MgFe_2O_4$ were analyzed. As shown in Figure 1c, the quantitative analysis determined that $MgFe_2O_4$ was formed

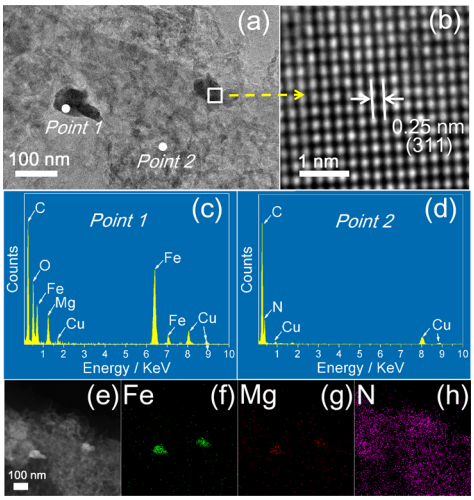

Figure 1. (a) TEM image of CN/MFO-150 photocatalyst. (b) High-resolution TEM image collected from the white square area in (a). Parts (c) and (d) are point scan profiles of EDX spectra acquired from point 1 ($MgFe_2O_4$ in CN/MFO-150) and point 2 (g-C_3N_4 in CN/MFO-150), respectively. (e) STEM image of CN/MFO-150 photocatalyst. (f)−(h) Elemental mappings of Fe, Mg, and N acquired from (e).

DOI: 10.1021/acsami.5b05714
ACS Appl. Mater. Interfaces 2015, 7, 18843−18848

with Mg/Fe = 1:2 and no N element was detected in *point 1*; while in Figure 1d, only C and N elements were detected, together suggesting that $MgFe_2O_4$ was dispersed onto the surface of g-C_3N_4. To evaluate the elemental distribution, the STEM (Figure 1e) and the elemental mapping of Fe, Mg, N species were performed for CN/MFO-150 as shown in Figure 1f–h. It can be observed that Mg, Fe, and O elements are homogeneously distributed in the $MgFe_2O_4$ area, confirming the existence of $MgFe_2O_4$; while N element from g-C_3N_4 is uniformly distributed in the areas without $MgFe_2O_4$. Furthermore, XPS results also confirmed the existence of $MgFe_2O_4$ in the CN/MFO-*X* photocatalysts by detecting Mg^{2+} (Mg 2p peak at 49.23 eV) and Fe^{3+} (Fe $2p_{3/2}$ peak at 710.5, Fe $2p_{1/2}$ peak at 724.2 eV, and Fe 3p peak at 55.73 eV), as shown in Figure S4. With the increasing amounts of $MgFe_2O_4$, the Mg and Fe XPS peak intensities were gradually increased, indicating the successful loading of $MgFe_2O_4$ onto the g-C_3N_4 surface. The Fe and Mg peaks were not detected in the CN/MFO-*X* (*X* = 30, 90) photocatalysts, mainly due to the detection limits of the XPS. The actual molar ratios of Mg/Fe were determined to be ca. 1:2 from the XPS quantitative analysis of the pure $MgFe_2O_4$, which was consistent with the EDX results. Furthermore, the actual weight ratio of $MgFe_2O_4$ in the CN/MFO-*X* (*X* = 30, 90, 150, 210, 300) were calculated to be 0.97 wt%, 2.18 wt%, 5.03 wt%, 8.13 wt%, and 10.34 wt% by taking the Fe contents as reference using X-ray fluorescence spectrometry (XRF), respectively (see all the element contents of the photocatalysts in Table S2).

The effect of $MgFe_2O_4$ particles on the photocatalytic performance for H_2 production over g-C_3N_4 was evaluated with Pt (1 wt %) loaded as the H_2 evolution catalyst by an in situ photoreduction method (see experimental details in the SI). As shown in Figure 2, with Pt loading, all the g-C_3N_4/$MgFe_2O_4$,

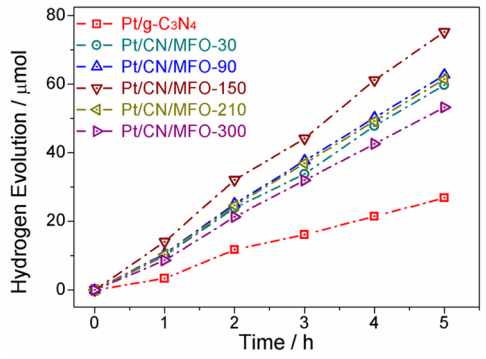

Figure 2. Time course of H_2 production over the as-prepared pure g-C_3N_4 and CN/MFO-*X* (*X* = 30, 90, 150, 210, 300) photocatalysts with 1 wt % Pt loading.

i.e., CN/MFO-*X* (*X* = 30, 90, 150, 210, 300) photocatalyst, showed much higher H_2 production activities as compared to g-C_3N_4. Note that the optimal photocatalyst was CN/MFO-150, more loaded $MgFe_2O_4$ will not always lead to better photocatalytic performance, which was mainly related to the shading effect[10,24,25,27] of the loaded $MgFe_2O_4$ covering the g-C_3N_4's active sites available for H_2 production. As shown in Figure S3, the larger surface area of g-C_3N_4 was covered with the increase of the loading amount of $MgFe_2O_4$, which will lead to a serious shading effect and hence a decrease in photocatalytic hydrogen production performance. As a consequence, the positive effect of $MgFe_2O_4$ would be offset by the negative shading effect of the large coverage of $MgFe_2O_4$ particles, leading to the optimal photocatalytic performance obtained at CN/MFO-150.

The optimal H_2 production rate over Pt/CN/MFO-150 was 30.09 μmol·h^{-1} (Figure 3), which was ~3 times as high as that

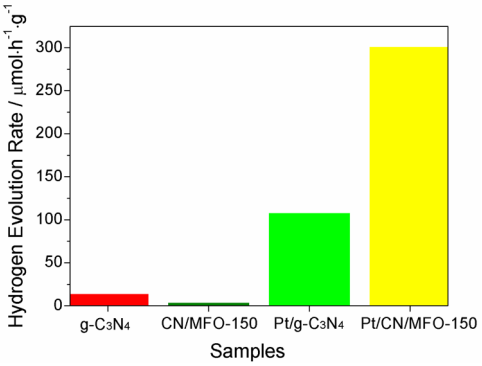

Figure 3. Visible light (λ > 420 nm) photocatalytic activity of water splitting H_2 production over g-C_3N_4 loaded with reduction cocatalyst Pt (1 wt %) and/or $MgFe_2O_4$.

of Pt/g-C_3N_4 photocatalysts. Remarkably, the apparent quantum efficiency at 420 nm irradiation was enhanced from 0.63% (g-C_3N_4) to 1.79% (CN/MFO-150). The turnover number (TON) over 5 hours hydrogen production in terms of g-C_3N_4 was determined to be 49.4 for pure g-C_3N_4 and 154.1 for CN/MFO-150, suggesting that the H_2 production arises from the photocatalytic process of g-C_3N_4 (see the TON of all the photocatalysts in Table S3). Thus, it can be deduced that $MgFe_2O_4$ can efficiently enhance the photocatalytic hydrogen production acitivity of g-C_3N_4 by improving charge separation in g-C_3N_4, given the inactivity of photocatalytic hydrogen evolution over $MgFe_2O_4$ itself even with Pt loading (data not shown).

However, one will find that the photocatalytic activity of g-C_3N_4/$MgFe_2O_4$ (without Pt loading, Figure 3) is quite poor, which is explainable when taking the band alignment of g-C_3N_4 and $MgFe_2O_4$ into consideration. The band gaps (E_g) of g-C_3N_4 and $MgFe_2O_4$ were determined to be 2.68 and 1.78 eV, respectively, from the UV–vis spectra of pure g-C_3N_4 and $MgFe_2O_4$ in Figure S5. The valence band maximum (VBM) positions of $MgFe_2O_4$ and g-C_3N_4 were measured to be about 1.79 and 2.39 eV below the Fermi level (E_f), respectively, based on the VB XPS results in Figure 4a. According to the formula $E_{CBM} = E_{VBM} - E_g$ (CBM: conduction band minimum), E_{CBM} of $MgFe_2O_4$ and g-C_3N_4 were calculated to be 0.01 eV below E_f and 0.29 eV above E_f, respectively. Consequently, as illustrated in the inset of Figure 4a, the E_{CBM} difference of 0.28 eV could facilitate the electron transfer from the CB of g-C_3N_4 to that of $MgFe_2O_4$; whereas the E_{VBM} difference of 0.60 eV will favor the hole transfer from the VB of g-C_3N_4 to that of $MgFe_2O_4$. Thus, this intrinsic straddling (Type I) band structures of g-C_3N_4 and $MgFe_2O_4$ could provide driving forces for the migration of photoinduced electrons and holes from g-C_3N_4 to $MgFe_2O_4$. Such a charge transfer process in g-C_3N_4/$MgFe_2O_4$ will induce electron–hole quenching and recombination at $MgFe_2O_4$, leading to poor photocatalytic activity of g-C_3N_4/$MgFe_2O_4$. To solidify this assumption on the charge transfer process, photoluminescence (PL, Figure S6) emission and time-resolved fluorescence emission decay spectra (Figure 4b) of pure g-C_3N_4 and CN/MFO-*X* were taken to determine how the type I band

DOI: 10.1021/acsami.5b05714
ACS Appl. Mater. Interfaces 2015, 7, 18843–18848

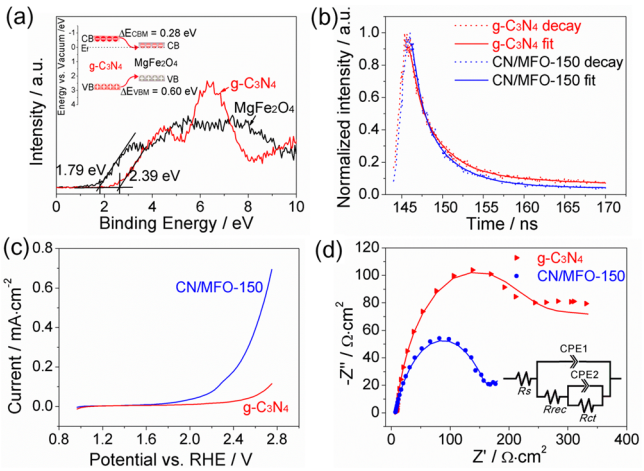

Figure 4. (a) Valence band XPS spectra of g-C_3N_4 and $MgFe_2O_4$. Inset: band alignment relationship between g-C_3N_4 and $MgFe_2O_4$. (b) Time-resolved fluorescence emission decay curves for g-C_3N_4 and CN/MFO-150 at room temperature. Observation wavelength for all the samples was 470 nm, and the excitation wavelength was 337 nm. Solid lines represent the kinetic fit using triexponential decay analysis. (c) Linear scan voltammogram (LSV) curves for g-C_3N_4 and CN/MFO-150 electrodes at an RDE (1600 rpm) in N_2-saturated 0.1 M KOH solution. Scan rate, 10 $mV \cdot s^{-1}$. (d) Nyquist impedance plots of the pure g-C_3N_4 and CN/MFO-150 electrodes measured in N_2-saturated 0.1 M KOH. The solid line traces correspond to the fitting using the equivalent circuit in the inset of (d).

alignment would affect the charge carrier behavior in the CN/MFO-*X* photocatalysts. The PL emission peaks centered at around 460 nm, and a tail extending to 700 nm, which could be attributed to the band−band irradiative recombination of photoinduced electrons and holes in g-C_3N_4.[10,24,25] The PL emission intensity exhibits the highest value for pure g-C_3N_4 and decreases with increasing $MgFe_2O_4$ contents, indicating that the bulk charge carriers recombination resulted from the band−band transition (process (*a*) in Figure 5) of g-C_3N_4 was

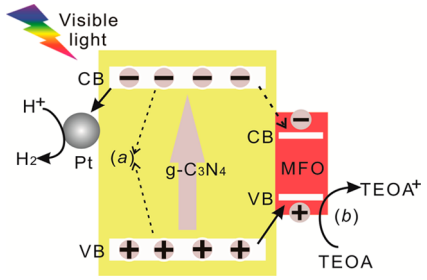

Figure 5. Proposed mechanism for photocatalystic hydrogen generation over Pt and $MgFe_2O_4$ loaded g-C_3N_4 photocatalyst. (CB: conduction band, VB: valence band, MFO: $MgFe_2O_4$, and TEOA: triethanolamine). Process (*a*): bulk charge carriers recombination in g-C_3N_4, (*b*): the oxidative reaction on the g-C_3N_4/$MgFe_2O_4$ surface. Solid arrow: major issue; dotted arrow: minor issue.

inhibited with $MgFe_2O_4$ loading. This suggests that the photoinduced electrons and/or holes in g-C_3N_4 would transfer to $MgFe_2O_4$. As shown in Figure 4b, evidently, the PL decay time of g-C_3N_4 was much shortened with $MgFe_2O_4$ loading, and the average lifetimes of the carriers (τ_{avg}) were determined to be 4.61 and 3.08 ns for g-C_3N_4 and CN/MFO-150, respectively (see decay kinetics calculation and parameters in Table S4). This suggests that $MgFe_2O_4$ particles can facilitate the electron transfer from g-C_3N_4 to $MgFe_2O_4$ by quenching the photoexcited state of g-C_3N_4,[28−30] which together with the PL spectra indicated that the photoinduced electrons and holes preferred to transfer to $MgFe_2O_4$ and then the reasons for the poor photocatalytic activity of g-C_3N_4/$MgFe_2O_4$ with type I band alignment were well explained.

As discussed above, in the g-C_3N_4/$MgFe_2O_4$ photocatalysts, both photoinduced electrons and holes preferred to transfer to $MgFe_2O_4$ which was incapable of photocatalytic H_2 production; and therefore, to ensure high photocatalytic activity, the electron transfer from g-C_3N_4 to $MgFe_2O_4$ must be prohibited while the holes were still kept to transfer from g-C_3N_4 to $MgFe_2O_4$ for efficient charge separation. Pt, a good hydrogen evolution catalyst, could entrap electrons photoinduced in semiconductors, which leads to effectively improved photocatalytic activity. In this study, Pt was loaded onto g-C_3N_4 and g-C_3N_4/$MgFe_2O_4$ photocatalysts, and as a result the photocatalytic activities were greatly enhanced, as shown in Figure 3. Then we can deduce that the charge transfer processes in Pt/g-C_3N_4/$MgFe_2O_4$ are quite different from those in g-C_3N_4/$MgFe_2O_4$. As illustrated in Figure 5, compared to g-C_3N_4/$MgFe_2O_4$ (inset of Figure 4a), the photoinduced electrons in g-C_3N_4 would prefer to transfer to Pt for H_2 production rather than exhaust at $MgFe_2O_4$ in the Pt/g-C_3N_4/$MgFe_2O_4$, emphasizing the importance of Pt as reductive hydrogen production catalyst; meanwhile, $MgFe_2O_4$ played an indispensable role of extracting the photoinduced holes out of g-C_3N_4. It is also noteworthy that Pt and $MgFe_2O_4$ nanoparticles are dispersed separately on the surface of g-C_3N_4 (Figure S7), again proving that Pt nanoparticles were mainly photoreduced by the photoelectrons from g-C_3N_4 instead of $MgFe_2O_4$. Hence, the photoinduced electrons and holes would flow to Pt and $MgFe_2O_4$, respectively, further leading to efficiently separated charge carriers and enhanced photocatalytic performance of g-C_3N_4.

In addition to the efficient charge transfer and separation in g-C_3N_4 as induced by $MgFe_2O_4$ together with Pt, the electrocatalysis effect of $MgFe_2O_4$ accelerating the oxidation reaction kinetics at the photocatalysts/electrolyte interfaces also contributed to the enhanced photocatalytic hydrogen evolution performance of Pt/g-C_3N_4/$MgFe_2O_4$ as compared to Pt/g-C_3N_4 (Figure 3). Herein, the catalytic oxidation abilities of pure g-C_3N_4 and g-C_3N_4/$MgFe_2O_4$ were compared by studying their electrocatalytic oxidation activities in oxygen evolution reaction (OER). Linear sweep voltammetry (LSV, Figure 4c) was performed to examine the electrocatalytic OER activities with the same amount of pure g-C_3N_4 and g-C_3N_4/$MgFe_2O_4$ loaded on the glassy carbon electrodes in a N_2-saturated 0.1 M KOH. Compared with pure g-C_3N_4 which has an onset potential of ca. 2.2 V vs RHE, the CN/MFO-150 shows a cathodic shift of the OER onset potential to be around 1.6 V vs RHE, inferring that the surface catalytic oxidative ability of g-C_3N_4 was greatly enhanced by loading $MgFe_2O_4$.[31−33] Note that actually no H_2 or O_2 was evolved over g-C_3N_4/$MgFe_2O_4$ in the pure water photocatalytic system (results not shown here), and the photocatalytic H_2 production reaction was indeed conducted in TEOA solutions instead of pure water, then LSV was also performed in a N_2-saturated 0.1 M KOH with 10 vol % TEOA to compare the electrocatalysis activities of g-C_3N_4 and CN/MFO-150 for the oxidation of TEOA, as shown in Figure S8. Due to the fact that TEOA acted as the hole sacrificial agent, which was much easier to be oxidized than OH^-, the onset potentials were greatly reduced with TEOA added in the

DOI: 10.1021/acsami.5b05714
ACS Appl. Mater. Interfaces 2015, 7, 18843−18848

electrolyte for both g-C_3N_4 and CN/MFO-150. Regardless, one can still find a ~53 mV cathodic shift of onset potential for TEOA oxidation reaction happened to CN/MFO-150 when compared to g-C_3N_4. Moreover, CN/MFO-150 had a higher current density at 2.0 V vs RHE (1.40 vs 0.65 mA·cm^{-2}) and a higher limiting current density (ca. 2.10 vs 0.66 mA·cm^{-2}) than g-C_3N_4, further proving that $MgFe_2O_4$ enhanced the surface catalytic oxidative ability of g-C_3N_4.

To better understand the oxidative electrocatalysis effect of $MgFe_2O_4$, electrochemical impedance spectroscopy (EIS) was performed at 2.5 V vs RHE in N_2-saturated 0.1 M KOH to elucidate the charge-transfer resistances in g-C_3N_4 and g-C_3N_4/$MgFe_2O_4$ (taking CN/MFO-150 as the representative electrode) electrodes. As shown in Figure 4d, the Nyquist impedance plots for these electrodes can be fitted to an equivalent circuit (Figure 4d, inset) consisting of R_s as the solution resistance of 0.1 M KOH electrolyte, the constant phase elements (CPE) associated with the semiconductor g-C_3N_4 (CPE1) and the loaded oxidative catalyst $MgFe_2O_4$ (CPE2), the internal recombination resistances in the electrodes (R_{rec}) and the charge-transfer resistances from the electrodes to the redox couples in the electrolyte (R_{ct}). The fitted parameters are summarized in Table S5. The charge-transfer resistance from CN/MFO-150 to electrolyte (53.99 Ω·cm^2) is dramatically lowered compared to that of the pure g-C_3N_4 (251.5 Ω·cm^2), confirming the facile electrode kinetics of CN/MFO-150[32] and further proving that $MgFe_2O_4$ loading can indeed enhance the catalytic oxidative kinetics. With $MgFe_2O_4$ loading, the internal recombination resistance in CN/MFO-150 (160.9 Ω·cm^2) is also smaller than that of pure g-C_3N_4 (228.6 Ω·cm^2), indicating that the g-C_3N_4/$MgFe_2O_4$ heterojunctions have intimate interfaces between g-C_3N_4 and the loaded $MgFe_2O_4$. These results are in good agreement with the observed superior oxidative performance of the CN/MFO-150 and highlight the benefits of loading $MgFe_2O_4$ as oxidative electrocatalyst on the g-C_3N_4 surface for enhanced water splitting performance.

To sum up, as illustrated in Figure 5, it thus can be deduced that $MgFe_2O_4$ not only can efficiently inhibit the bulk charge carrier recombination (process (*a*) in Figure 5) in g-C_3N_4 by extracting the photoinduced holes out of g-C_3N_4 due to the more negative VB position of $MgFe_2O_4$ than g-C_3N_4, but also accelerate the oxidative reaction kinetics on the surface of g-C_3N_4/$MgFe_2O_4$ (process (*b*) in Figure 5). With Pt loading as HEC, the photoinduced electrons and holes were entrapped by Pt and $MgFe_2O_4$, respectively, giving rise to the promoted charge separation in the Pt/g-C_3N_4/$MgFe_2O_4$ photocatalyst. Therefore, the roles of Pt and $MgFe_2O_4$ were clearly defined so that Pt functioned as reductive hydrogen production sites, while $MgFe_2O_4$ bifunctioned to separate charge carriers in g-C_3N_4 and accelerate the oxidative reaction kinetics on g-C_3N_4, leading to stable (Figure S9) and drastically enhanced photocatalytic hydrogen production performance of Pt/g-C_3N_4/$MgFe_2O_4$.

3. CONCLUSIONS

The visible light photocatalytic hydrogen production activity of g-C_3N_4 was greatly enhanced with bifunctional $MgFe_2O_4$ modification. It was revealed that with $MgFe_2O_4$ loading, the photoinduced charge carriers were efficiently separated at the g-C_3N_4/$MgFe_2O_4$ interface, and the surface oxidative reaction kinetics of g-C_3N_4/$MgFe_2O_4$ was also accelerated compared to the pure g-C_3N_4. Together with Pt loading as reductive hydrogen production sites, efficient charge carriers were achieved, leading to considerably high photocatalytic hydrogen production performance. This study demonstrated the important role of bifunctional $MgFe_2O_4$ loaded onto the surface of g-C_3N_4 toward efficient water splitting hydrogen production, which might open up an alternative method to develop novel heterostructures for efficient solar fuel conversion.

■ ASSOCIATED CONTENT

Supporting Information

The Supporting Information is available free of charge on the ACS Publications website at DOI: 10.1021/acsami.5b05714.

The experimental section, XRD patterns, BET surface areas and pore distribution results, XRF quantitative detection results, TEM images and XPS of all the photocatalysts, UV−vis of $MgFe_2O_4$ and g-C_3N_4, PL spectra of the photocatalysts, TEM and mapping of Pt/g-C_3N_4/$MgFe_2O_4$, LSV of g-C_3N_4, CN/MFO-150 with or without TEOA in the electrolyte, fitted values of the EIS parameters, photocatalytic stability test of CN/MFO-150 (PDF)

■ AUTHOR INFORMATION

Corresponding Author

*E-mail: shshen_xjtu@mail.xjtu.edu.cn (S.S.).

Author Contributions

The manuscript was written through contributions of all authors. All authors have given approval to the final version of the manuscript. S.S. and L.G. designed the study. J.C. prepared and characterized all the samples. S.S. and J.C. wrote the article, D.Z. helped with the hydrogen production test, Z.D. and M.W. contributed to the electrochemical test. This work was done under the guidance of S.S. and L.G.

Notes

The authors declare no competing financial interest.

■ ACKNOWLEDGMENTS

The authors gratefully acknowledge the financial support from the National Natural Science Foundation of China (No. 51323011, No. 51236007), the Program for New Century Excellent Talents in University (No. NCET-13-0455), the Natural Science Foundation of Shaanxi Province (No. 2014KW07-02), the Natural Science Foundation of Jiangsu Province (No. BK20141212), and the Nano Research Program of Suzhou City (No. ZXG201442, No. ZXG2013003). S.S. was supported by the Foundation for the Author of National Excellent Doctoral Dissertation of China (No. 201335) and the "Fundamental Research Funds for the Central Universities."

■ REFERENCES

(1) Chen, X.; Shen, S.; Guo, L.; Mao, S. S. Semiconductor-based Photocatalytic Hydrogen Generation. *Chem. Rev.* **2010**, *110*, 6503−6570.

(2) Akihiko, K.; Yugo, M. Heterogeneous Photocatalyst Materials for Water Splitting. *Chem. Soc. Rev.* **2009**, *38*, 253−278.

(3) Fujishima, A.; Honda, K. Electrochemical Photolysis of Water at a Semiconductor Electrode. *Nature* **1972**, *238*, 37−38.

(4) Yang, J. H.; Wang, D. G.; Han, H. X.; Li, C. Roles of Cocatalysts in Photocatalysis and Photoelectrocatalysis. *Acc. Chem. Res.* **2013**, *46*, 1900−1909.

(5) Wang, X.; Maeda, K.; Thomas, A.; Takanabe, K.; Xin, G.; Carlsson, J. M.; Domen, K.; Antonietti, M. A Metal-free Polymeric

DOI: 10.1021/acsami.5b05714
ACS Appl. Mater. Interfaces 2015, 7, 18843−18848

Photocatalyst for Hydrogen Production from Water under Visible Light. *Nat. Mater.* **2009**, *8*, 76−80.
(6) Liu, J.; Liu, Y.; Liu, N. Y.; Han, Y. Z.; Zhang, X.; Huang, H.; Lifshitz, Y.; Lee, S.-T.; Zhong, J.; Kang, Z. H. Metal-free Efficient Photocatalyst for Stable Visible Water Splitting via a Two-electron Pathway. *Science* **2015**, *347*, 970−974.
(7) Wang, X.; Blechert, S.; Antonietti, M. Polymeric Graphitic Carbon Nitride for Heterogeneous Photocatalysis. *ACS Catal.* **2012**, *2*, 1596−1606.
(8) Zhang, J.; Zhang, M.; Sun, R. Q.; Wang, X. A Facile Band Alignment of Polymeric Carbon Nitride Semiconductors to Construct Isotype Heterojunctions. *Angew. Chem.* **2012**, *124*, 10292−10296.
(9) Maeda, K.; Wang, X.; Nishihara, Y.; Lu, D.; Antonietti, M.; Domen, K. Photocatalytic Activities of Graphitic Carbon Nitride Powder for Water Reduction and Oxidation Under Visible Light. *J. Phys. Chem. C* **2009**, *113*, 4940−4947.
(10) Hou, Y. D.; Laursen, A. B.; Zhang, J. S.; Zhang, G. G.; Zhu, Y. S.; Wang, X. C.; Dahl, S.; Chorkendorff, I. Layered Nanojunctions for Hydrogen-Evolution Catalysis. *Angew. Chem., Int. Ed.* **2013**, *52*, 3621−3625.
(11) Xu, J; Li, Y. X.; Peng, S. Q. Photocatalytic Hydrogen Evolution over Erythrosin B-Sensitized Graphitic Carbon Nitride with in situ Grown Molybdenum Sulfide Cocatalyst. . *Int. J. Hydrogen Energy* **2015**, *40*, 353−362.
(12) Cheng, C.; Amini, A.; Zhu, C.; Xu, Z. L.; Song, H. S.; Wang, N. Enhanced Photocatalytic Performance of TiO_2-ZnO Hybrid Nanostructures. *Sci. Rep.* **2014**, *4*, 4181.
(13) Zheng, Z. K.; Xie, W.; Lim, Z. S.; You, L.; Wang, J. L. CdS Sensitized 3D Hierarchical TiO_2/ZnO Heterostructure for Efficient Solar Energy Conversion. *Sci. Rep.* **2014**, *4*, 5721.
(14) Wu, K. F.; Chen, Z. Y.; Lv, H. J.; Zhu, H. M.; Hill, C. L.; Lian, T. Q. Hole Removal Rate Limits Photodriven H_2 Generation Efficiency in CdS-Pt and CdSe/CdS-Pt Semiconductor Nanorod-Metal Tip Heterostructures. *J. Am. Chem. Soc.* **2014**, *136*, 7708−7716.
(15) Thibert, A.; Frame, F. A.; Busby, E.; Holmes, M. A.; Osterloh, F. E.; Larsen, D. S. Sequestering High-energy Electrons to Facilitate Photocatalytic Hydrogen Generation in CdSe/CdS Nanocrystals. *J. Phys. Chem. Lett.* **2011**, *2*, 2688−2694.
(16) Peng, S. Q.; Huang, Y. H.; Li, Y. X. Rare Earth Doped TiO_2-CdS and TiO_2-CdS Composites with Improvement of Photocatalytic Hydrogen Evolution under Visible Light Irradiation. *Mater. Sci. Semicond. Process.* **2013**, *16*, 62−69.
(17) Chen, J.; Shen, S. H.; Guo, P. H.; Wang, M.; Wu, P.; Wang, X. X.; Guo, L. J. In-situ Reduction Synthesis of Nano-sized Cu_2O Particles Modifying g-C_3N_4 for Enhanced Photocatalytic Hydrogen Production. *Appl. Catal., B* **2014**, *152*−*153*, 335−341.
(18) Chen, J.; Shen, S. H.; Wu, P.; Guo, L. J. Nitrogen-doped CeO_x Nanoparticles Modified Graphitic Carbon Nitride for Enhanced Photocatalytic Hydrogen Production. *Green Chem.* **2015**, *17*, 509−517.
(19) Li, Y.X.; Wang, H.; Peng, S. Q. Tunable Photodeposition of MoS2 onto a Composite of Reduced Graphene Oxide and CdS for Synergic Photocatalytic Hydrogen Generation. . *J. Phys. Chem. C* **2014**, *118*, 19842−19848.
(20) Hou, Y.; Zuo, F.; Dagg, A.; Feng, P. A Three-Dimensional Branched Cobalt-Doped α-Fe_2O_3 Nanorod/$MgFe_2O_4$ Heterojunction Array as a Flexible Photoanode for Efficient Photoelectrochemical Water Oxidation. *Angew. Chem., Int. Ed.* **2013**, *52*, 1248−1252.
(21) Kim, E.; Nishimura, N.; Magesh, G.; Kim, J. Y.; Jang, J.-W.; Jun, H.; Kubota, J.; Domen, K.; Lee, J. S. Fabrication of $CaFe_2O_4$/TaON Heterojunction Photoanode for Photoelectrochemical Water Oxidation. *J. Am. Chem. Soc.* **2013**, *135*, 5375−5383.
(22) McDonald, K.; Choi, K. Synthesis and Photoelectrochemical Properties of Fe_2O_3/$ZnFe_2O_4$ Composite Photoanodes for Use in Solar Water Oxidation. *Chem. Mater.* **2011**, *23*, 4863−4869.
(23) Kim, H. G.; Borse, P. H.; Jang, J. S.; Jeong, E. D.; Jung, O.-S.; Suh, Y. J.; Lee, J. S. Fabrication of $CaFe_2O_4$/$MgFe_2O_4$ Bulk Heterojunction for Enhanced Visible Light Photocatalysis. *Chem. Commun.* **2009**, 5889−5891.
(24) Niu, P.; Zhang, L.; Liu, G.; Cheng, H.-M. Graphene-Like Carbon Nitride Nanosheets for Improved Photocatalytic Activities. *Adv. Funct. Mater.* **2012**, *22*, 4736−4770.
(25) Niu, P.; Yang, Y. Q.; Yu, J. C.; Liu, G.; Cheng, H.-M. Switching the Selectivity of the Photoreduction Reaction of Carbon Dioxide by Controlling the Band Structure of a g-C_3N_4 Photocatalyst. *Chem. Commun.* **2014**, *50*, 10837−10840.
(26) Li, Y. B.; Zhang, H. M.; Liu, P. R.; Wang, D.; Li, Y.; Zhao, H. J. Cross-Linked g-C_3N_4/rGO Nanocomposites with Tunable Band Structure and Enhanced Visible Light Photocatalytic Activity. *Small* **2013**, *9*, 3336−3344.
(27) Wang, M. Y.; Sun, L.; Lin, Z. Q.; Cai, J. H.; Xie, K. P.; Lin, C. J. P-N Heterojunction Photoelectrodes Composed of Cu_2O-loaded TiO_2 Nanotube Arrays with Enhanced Photoelectrochemical and Photoelectrocatalytic Activities. *Energy Environ. Sci.* **2013**, *6*, 1211−1220.
(28) Chen, J.; Shen, S. H.; Guo, P. H.; Wu, P.; Guo, L. J. Spatial Engineering of Photo-active Sites on g-C_3N_4 for Efficient Solar Hydrogen Generation. *J. Mater. Chem. A* **2014**, *2*, 4605−4612.
(29) Xu, J. Y.; Li, Y. X.; Peng, S. Q.; Lu, G. X.; Li, S. B. Eosin Y-sensitized Graphitic Carbon Nitride Fabricated by Heating Urea for Visible Light Photocatalytic Hydrogen Evolution: the Effect of the Pyrolysis Temperature of Urea. *Phys. Chem. Chem. Phys.* **2013**, *15*, 7657−7665.
(30) Zhang, Z. Y.; Huang, J. D.; Zhang, M. Y.; Yuan, Q.; Dong, B. Ultrathin Hexagonal SnS_2 Nanosheets Coupled with g-C_3N_4 Nanosheets as 2D/2D Heterojunction Photocatalysts toward High Photocatalytic Activity. *Appl. Catal., B* **2015**, *163*, 298−305.
(31) Ding, Q.; Meng, F.; English, C. R.; Cabán-Acevedo, M.; Shearer, M. J.; Liang, D.; Daniel, A. S.; Hamers, R. J.; Jin, S. Efficient Photoelectrochemical Hydrogen Generation Using Heterostructures of Si and Chemically Exfoliated Metallic MoS_2. *J. Am. Chem. Soc.* **2014**, *136*, 8504−8507.
(32) Mao, S.; Wen, Z. H.; Huang, T. Z.; Hou, Y.; Chen, J. H. High-performance Bi-functional Electrocatalysts of 3D Crumpled Graphene-cobalt Oxide Nanohybrids for Oxygen Reduction and Evolution Reactions. *Energy Environ. Sci.* **2014**, *7*, 609−616.
(33) Hong, Y.-R.; Liu, Z. L.; Al-Bukhari, S. F. B. S. A.; Lee, C. J. J.; Yung, D. L.; Chi, D. Z.; Andy Hor, T. S. Effect of Oxygen Evolution Catalysts on Hematite Nanorods for Solar Water Oxidation. *Chem. Commun.* **2011**, *47*, 10653−10655.

DOI: 10.1021/acsami.5b05714
ACS Appl. Mater. Interfaces 2015, 7, 18843−18848